IEEE Access
Multidisciplinary | Rapid Review | Open Access Journal

Received December 6, 2018, accepted December 14, 2018, date of publication December 19, 2018,
date of current version January 11, 2019.

Digital Object Identifier 10.1109/ACCESS.2018.2888584

Finite-Difference Time-Domain Modeling for Electromagnetic Wave Analysis of Human Voxel Model at Millimeter-Wave Frequencies

JAE-WOO BAEK[1], DONG-KYOO KIM[2], AND KYUNG-YOUNG JUNG[1], (Senior Member, IEEE)

[1]Department of Electronics and Computer Engineering, Hanyang University, Seoul 04763, South Korea
[2]Hyper-Connected Communication Research Laboratory, Electronics and Telecommunications Research Institute, Daejeon 34129, South Korea

Corresponding author: Kyung-Young Jung (kyjung3@hanyang.ac.kr)

This work was supported in part by the Electronics and Telecommunications Research Institute (ETRI) Grant through the Korean Government (MSIT) (Robust Contactless Wearable Radar Technology with Motion Artifact Removal for Easy-to-Wear Vital-Sign Sensing Devices) under Grant 18ZH1600 and in part by the Institute for Information and Communications Technology Promotion (IITP) Grant through the Korean Government (MSIT) (Cloud-Based SW Platform Development for RF Design and EM Analysis) under Grant 2016-0-00130.

ABSTRACT The finite-difference time-domain (FDTD) modeling of a human voxel model at millimeter-wave (mmWave) frequencies is presented. It is very important to develop the proper geometrical and electrical modeling of a human voxel model suitable for accurate electromagnetic (EM) analysis. Although there are many human phantom models available, their voxel resolution is too poor to use for the FDTD study of EM wave interaction with human tissues. In this paper, we develop a proper human voxel model suitable for mmWave FDTD analysis using the voxel resolution enhancement technique and the image smoothing technique. The former can improve the resolution of the human voxel model and the latter can alleviate staircasing boundaries of the human voxel model. Quadratic complex rational function is employed for the electrical modeling of human tissues in the frequency range of 6–100 GHz. Massage passing interface-based parallel processing is also applied to dramatically speed up FDTD calculations. Numerical examples are used to illustrate the validity of the mmWave FDTD simulator developed here for bio electromagnetics studies.

INDEX TERMS Finite-difference time-domain (FDTD) method, electromagnetic wave, human tissue, dispersion model, parallel processing, bioelectromagnetics, Doppler radar.

I. INTRODUCTION

During the past few decades, the use of electromagnetic (EM) wave has been explosively increasing in the wide range of applications such as wireless communication, biomedical applications, etc. Operating frequencies are also rapidly increasing because they can provide great advantages. For wireless communication technology, high operating frequency bands are preferred owing to the need of high bit rates and compact size. In the new generation wireless communication system [1], millimeter-wave (mmWave) bands (28 GHz, 38 GHz, 64 GHz, and 71 GHz) will be of significant importance [2]. Note that the study of 5G channel modeling was performed in the frequency range from 6 GHz to 100 GHz [3]. For biomedical applications, EM waves has been popularly utilized for cancer detection [4]–[6]. For example, the study on the electrical modeling of breast cancer was performed in the frequency range of 500 MHz to 20 GHz [7] and the effective medium theory was employed for the electrical modeling of skin cancer from 20 GHz to 100 GHz [8]. In addition, Doppler radars has been actively utilized for remote monitoring of human vital signs in the 24 GHz and 60 GHz band [9]. Therefore, it is of great necessary to investigate EM wave interaction with human body at these high frequencies.

Due to the lack of analytical EM solutions in human body that has complex, inhomogeneous, and dispersive characteristics, numerical methods play a vital role in the study of EM wave propagation in human tissues. Among computational electromagnetics, the finite-difference time-domain (FDTD) method [10]–[12] is very popular for bioelectromagnetics [13]–[18] because it is robust, versatile, simple to implement, and also it can obtain wideband responses in a single run [19]–[23]. In this work, we develop FDTD modeling suitable for EM wave analysis of a computational human voxel phantom in the frequency range of 6–100 GHz that

covers the above-mentioned frequency bands. It is well known that FDTD cell size should be chosen as at least 10–20 point per wavelength (PPW) for computational accuracy [11]. Since 1988, many human voxel phantoms have been reported in the literature: BABY with the voxel resolution of 0.85 mm × 0.85 mm × 4 mm [24], VoxelMan with the voxel resolution of 1 mm × 1 mm × 0.5 mm [25], VIP-MAN with the voxel resolution of 0.33 mm × 0.33 mm × 1 mm [26], Nagaoga with the voxel resolution of 2 mm × 2 mm × 2 mm [27], KORMAN with the voxel resolution of 2 mm × 2 mm × 5 mm [28], Katja with the voxel resolution of 1.775 mm × 1.775 mm × 4.8 mm [29], CNMAN with the voxel resolution of 0.16 mm × 0.16 mm × 0.5 mm [30], Virtual Population with the voxel resolution of 0.5 mm × 0.5 mm × 0.5 mm [31], Rad-Human with the voxel resolution of 0.15 mm × 0.15 mm × 0.25 mm [32], and Visible Korean with the voxel resolution of 1 mm × 1 mm × 1 mm [33]. However, all existing computational human phantoms do not meet the requirement of FDTD voxel size in the frequency range of interest. For Rad-Human model (to our best knowledge, it provides the highest voxel resolution), its PPW is only 3.33 for cerebrospinal fluid at 100 GHz. In other words, when employing the Rad-Human model, the maximum usable frequency for EM analysis is 26.2 GHz under the FDTD voxel resolution guideline of 10 PPW and it is only 10.5 GHz under the 20 PPW guideline. Therefore, it is of great necessity to develop a high-resolution human voxel model in the frequency of interest. Based on the voxel resolution enhancement method, we develop the human voxel model with the voxel resolution of 0.025 mm × 0.025 mm × 0.025 mm, leading to 33.32 PPW for the cerebrospinal fluid at 100 GHz. However, this resolution-improved human voxel phantom has the same shape of large staircasing boundaries as the original human phantom, albeit with meeting the FDTD voxel resolution requirement. To alleviate staircasing boundaries of the human voxel model, the image smoothing method [34] is employed in this study. To our best knowledge, it is the first time to incorporate the voxel resolution enhancement technique and the image smoothing technique simultaneously to obtain a high-resolution human voxel model suitable for mmWave FDTD analysis. Before proceeding, it should be mentioned that voxel-based human models can represent inhomogeneity of human tissues simply and also show human tissues exactly as the source images. That explains why FDTD is so popular for EM analysis of a human model. On the other hand, other numerical methods such as the method of moment (MoM) [35] and the finite element method (FEM) [36] rely on unstructured meshes and thus it is not straightforward to apply these methods to analyze EM wave interaction with a human model. There is limited literature on unstructured meshes of a human model for EM analysis [37], [38].

As previously alluded to, human tissues have dispersion characteristics: their dielectric properties vary with the frequency. Therefore, accurate dispersive modeling should be applied for the human voxel model. In this work, a quadratic complex rational function (QCRF) [39] is employed for the electrical modeling of human tissues in the frequency range of 6–100 GHz. It is worth noting that the FDTD algorithm does not involve matrix calculations differently from MoM and FEM, thus easily implementing its parallel programming. Massage passing interface (MPI) parallel programming [40] is utilized to FDTD simulations [41] in this work. The remainder of this paper is organized as follows. We first present the accurate geometrical modeling of a human voxel model suitable for mmWave FDTD analysis based on the voxel resolution enhancement method and the image smoothing method. Next, QCRF-FDTD algorithm and MPI implementation are provided for proper electrical modeling and computational speedup respectively. Numerical examples in one-dimensional (1-D) and three dimensional (3-D) are used to validate our work. Finally, concluding remarks are provided.

II. MMWAVE FDTD MODELING

In what follows, the time dependence of $e^{\mathrm{j}\omega t}$ is assumed, where $\mathrm{j} = \sqrt{-1}$. The discrete representation of field $f(x, y, z, t)$ is defined as $f(i\Delta x, j\Delta y, k\Delta z, n\Delta t) = f^n(i, j, k)$, where i, j, and k refer to the spatial grid indexing, n refers to the time step indexing, Δs ($s = x, y, z$) is the spatial cell size in the s-direction, and Δt is the time step size.

A. HIGH-RESOLUTION HUMAN VOXEL MODEL

In this section, a high-resolution human voxel model is developed for EM wave analysis at mmWave frequencies. As a proof of concept, we consider some brain part of *Ella*, a female phantom model with the voxel resolution of 0.5 mm × 0.5 mm × 0.5 mm, from Virtual Population [31] (one of the most popular human phantom models), referred to as an original human phantom model (Fig. 1). As explained previously, its voxel resolution should be improved to meet the requirement of FDTD voxel size in the frequency range of interest. The development of a high-resolution human voxel phantom is composed of the voxel resolution enhancement method and the image smoothing method.

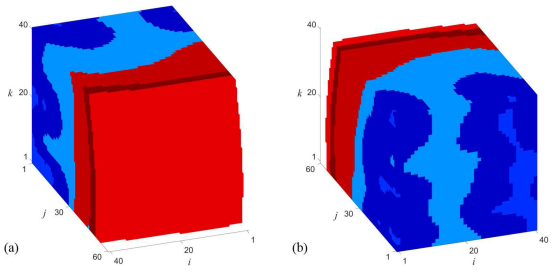

FIGURE 1. Original human voxel model with the voxel resolution of 0.5 mm × 0.5 mm × 0.5 mm and it has 40 × 60 × 40 voxels. (a) Front-side view. (b) Back-side view. Voxel coloring: ■ skin, ■ subcutaneous adipose tissue (SAT), ■ skull, ■ cerebrospinal fluid, ■ brain gray matter, and ■ brain white matter.

For the first step, the voxel resolution enhancement can be performed by downsizing the FDTD cell and its process can be given by the following

$$V_O(i \times R + ii, j \times R + jj, k \times R + kk) \leftarrow V_I(i, j, k), \quad 0 \leq ii, jj, kk < R. \tag{1}$$

Here, V_I and V_O represent an integer array of media information allocated to the input (original) human voxel model and the output (resolution-improved) human voxel model, respectively. For example, air is set as 0, brain gray matter as 2, brain white matter as 5, cerebrospinal fluid as 8, etc. The resolution enhancement ratio is defined as R. By performing this process, we can obtain fine FDTD cell size (Δs_O) from the original coarse FDTD cell size (Δs_I). Note that $R = \Delta s_I / \Delta s_O$ and we set $R = 20$ in this work, leading to the human phantom with voxel resolution of 0.025 mm $\times$ 0.025 mm $\times$ 0.025 mm. Although the resulting human voxel phantom can meet the voxel resolution guideline for FDTD accuracy, it still keeps the shape of large staircasing boundaries as the original human voxel phantom as shown in Fig 2.

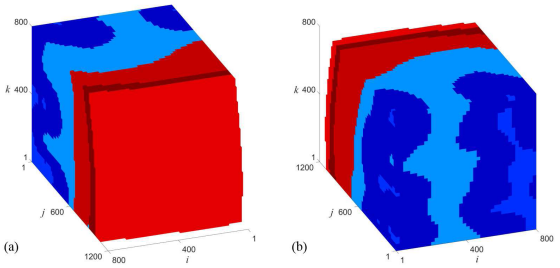

FIGURE 2. Human voxel model with the voxel resolution of 0.025 mm × 0.025 mm × 0.025 mm and it has 800 × 1200 × 800 voxels. Subcaptions and voxel coloring are same as Fig. 1.

For the next step, to alleviate staircasing boundaries, the image smoothing method that is usually utilized in the imaging processing technique is employed [34]. The image smoothing technique that we apply in this work consists of four-substep procedures:

Step 1: Opening with the octahedron structuring element
Step 2: Closing with the octahedron structuring element
Step 3: Opening with the spherical structuring element
Step 4: Closing with the spherical structuring element

The opening and closing processes involve erosion and dilation. The erosion operation of the media information image V_O by a structuring element B is given by the following

$$[V_O \ominus B](i, j, k) = \min_{(p,q,r) \in B} \{V_O(i + p, j + q, k + r)\}. \tag{2}$$

The dilation operation is given by the following

$$[V_O \oplus B](i, j, k) = \max_{(p,q,r) \in B} \{V_O(i - p, j - q, k - r)\}. \tag{3}$$

Now, the opening process and the closing process can be performed by

$$V_O \circ B = (A \ominus B) \oplus B \tag{4}$$

$$V_O ¥ B = (A \oplus B) \ominus B, \tag{5}$$

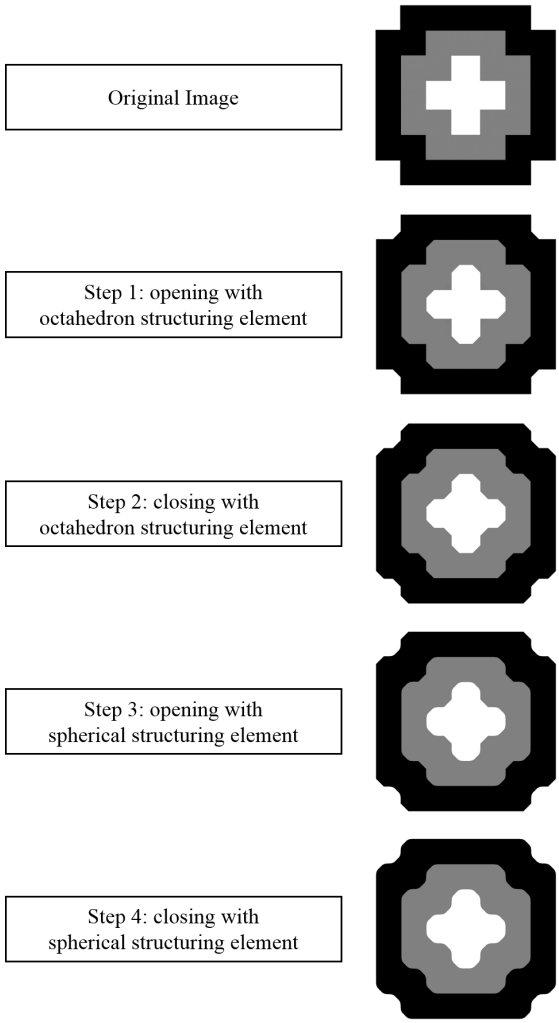

FIGURE 3. Image smoothing method for a 2-D simple structure.

respectively. To clearly illustrate how the each substep process works, we consider a simple two-dimensional (2-D) structure. Fig. 3 shows the flow chart of the image smoothing technique utilized in this work and the resulting image for each substep process. Fig. 4 shows the high-resolution FDTD human voxel model after applying the above-mentioned image smoothing method. As shown in the figure, the image smoothing technique can significantly mitigate staircasing boundaries of the human phantom model, compared to Fig. 2. It is believed that proposed geometrical modeling is very well suitable for FDTD analysis of the human voxel model at mmWave frequencies.

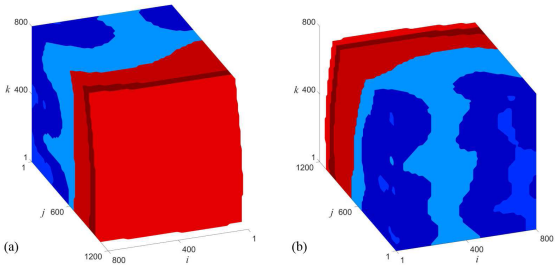

FIGURE 4. Final high-resolution human voxel model with the voxel resolution suitable for mmWave FDTD analysis. Subcaptions and voxel coloring are same as Fig. 1.

B. MMWAVE DISPERSIVE FDTD ALGORITHM

As mentioned previously, dielectric properties of human tissues vary with the frequency, thus needing a proper dispersion model of the FDTD human voxel model in the frequency of interest. Debye, Lorentz, and Drude dispersion models are interesting for representing dielectric characteristics of materials of interest [42], [43]. However, a complicated optimization technique should be used to obtain accurate coefficients, which implies that some initial values may often lead to inadequate coefficients [42] because the coefficient solution space is too large (usually in the range of more than 8 orders of magnitude). QCRF dispersion model was successfully used for FDTD analysis of complex media in the wide range of applications such as human tissues in 0.4–3 GHz [39], concrete materials in 50–1000 MHz [44], amorphous silicon/crystalline silicon solar cells in 300–1000 THz [45], and plasmonic nanoparticles in 300–1000 THz [46]. Note that QCRF dispersion model is more efficient and accurate than Debye, Lorentz, and Drude dispersion models because it has more degrees of freedom. In QCRF dispersion model, the relative permittivity is expressed as follows [39]

$$\varepsilon_r(\omega) = \frac{A_0 + A_1(\jmath\omega) + A_2(\jmath\omega)^2}{B_0 + B_1(\jmath\omega) + B_2(\jmath\omega)^2}, \tag{6}$$

where A_0, A_1, A_2, B_0, B_1, and B_2 are the real-numbered coefficients (for simplicity, we set $B_0 = 1$). Appropriate QCRF coefficients can be obtained using the complex curve fitting method [47], [48].

In QCRF-FDTD, the update equation for electric field (**E**) is obtained using the constitutive relation, the inverse Fourier transform, and the central difference scheme:

$$\mathbf{E}^{n+1} = c_1\mathbf{E}^n + c_2\mathbf{E}^{n-1} + c_3\mathbf{D}^{n+1} + c_4\mathbf{D}^n + c_5\mathbf{D}^{n-1}, \tag{7}$$

where update equation coefficients are

$$\begin{aligned} c_1 &= 2\frac{\alpha_2 - \alpha_0}{\alpha_0 + \alpha_1 + \alpha_2} \\ c_2 &= \frac{\alpha_1 - \alpha_0 - \alpha_2}{\alpha_0 + \alpha_1 + \alpha_2} \\ c_3 &= \frac{\beta_0 + \beta_1 + \beta_2}{\alpha_0 + \alpha_1 + \alpha_2} \\ c_4 &= 2\frac{\beta_0 - \beta_2}{\alpha_0 + \alpha_1 + \alpha_2} \\ c_5 &= \frac{\beta_0 - \beta_1 + \beta_2}{\alpha_0 + \alpha_1 + \alpha_2}. \end{aligned}$$

Here, $\alpha_0 = A_0\Delta t^2$, $\alpha_1 = 2A_1\Delta t$, $\alpha_2 = 4A_2$, $\beta_0 = \Delta t^2/\varepsilon_0$, $\beta_1 = 2B_1\Delta t/\varepsilon_0$, and $\beta_2 = 4B_2/\varepsilon_0$. It is stressed that the memory requirement can be reduced from five real-valued arrays to four real-valued arrays using a transposed direct Form II structure [49] as known in the signal processing literature. Update equations for magnetic field (**H**) and electric flux density (**D**) can be simply obtained by the standard Yee discretization of Ampere's law and Faraday's law [11], [50]. Note that an absorbing boundary condition should employed be to terminate the computational space because FDTD is developed based on partial difference equation. Material-independent perfectly matched layer (PML) can be incorporated in QCRF-FDTD, based on the stretched coordinate approach [51], [52]. For example, final update equations for H_x and D_x can be written as (8) and (9), as

$$\begin{aligned} H_x^{n+\frac{1}{2}}\left(i, j+\frac{1}{2}, k+\frac{1}{2}\right) &= H_x^{n-\frac{1}{2}}\left(i, j+\frac{1}{2}, k+\frac{1}{2}\right) - \frac{\Delta t}{\mu\Delta y}\left[E_z^n\left(i, j+1, k+\frac{1}{2}\right) - E_z^n\left(i, j, k+\frac{1}{2}\right)\right] \\ &\quad + \frac{\Delta t}{\mu\Delta z}\left[E_y^n\left(i, j+\frac{1}{2}, k+1\right) - E_y^n\left(i, j+\frac{1}{2}, k\right)\right] \\ &\quad + \frac{\Delta t}{2\mu}\left[G_{xy}^{n+\frac{1}{2}}\left(i, j+\frac{1}{2}, k+\frac{1}{2}\right) + G_{xy}^{n-\frac{1}{2}}\left(i, j+\frac{1}{2}, k+\frac{1}{2}\right)\right] \\ &\quad - \frac{\Delta t}{2\mu}\left[G_{xz}^{n+\frac{1}{2}}\left(i, j+\frac{1}{2}, k+\frac{1}{2}\right) + G_{xz}^{n-\frac{1}{2}}\left(i, j+\frac{1}{2}, k+\frac{1}{2}\right)\right] \end{aligned} \tag{8}$$

$$\begin{aligned} D_x^{n+1}\left(i+\frac{1}{2}, j, k\right) &= D_x^n\left(i+\frac{1}{2}, j, k\right) + \frac{\Delta t}{\Delta y}\left[H_z^{n+\frac{1}{2}}\left(i+\frac{1}{2}, j+\frac{1}{2}, k\right) - H_z^{n+\frac{1}{2}}\left(i+\frac{1}{2}, j-\frac{1}{2}, k\right)\right] \\ &\quad - \frac{\Delta t}{\Delta z}\left[H_y^{n+\frac{1}{2}}\left(i+\frac{1}{2}, j, k+\frac{1}{2}\right) - H_y^{n+\frac{1}{2}}\left(i+\frac{1}{2}, j, k+\frac{1}{2}\right)\right] \\ &\quad - \frac{\Delta t}{2}\left[F_{xy}^{n+1}\left(i+\frac{1}{2}, j, k\right) + F_{xy}^n\left(i+\frac{1}{2}, j, k\right)\right] + \frac{\Delta t}{2}\left[F_{xz}^{n+1}\left(i+\frac{1}{2}, j, k\right) + F_{xz}^n\left(i+\frac{1}{2}, j, k\right)\right] \end{aligned} \tag{9}$$

TABLE 1. Quadratic complex rational function dispersive modelling of human tissues in the frequency range of 6–100 GHz.

	skin	SAT	skull	cerebrospinal fluid	brain gray matter	brain white matter	cord	blood	heart
A_0	45.26	5.47	12.25	76.64	52.00	37.82	31.61	62.62	66.74
A_1	2.00×10^{-09}	6.69×10^{-11}	1.39×10^{-10}	9.74×10^{-10}	4.64×10^{-10}	3.36×10^{-10}	2.61×10^{-10}	6.60×10^{-10}	8.06×10^{-10}
A_2	1.54×10^{-21}	1.21×10^{-22}	1.98×10^{-22}	5.30×10^{-22}	2.91×10^{-22}	2.57×10^{-22}	2.18×10^{-22}	3.42×10^{-22}	5.05×10^{-22}
B_1	5.98×10^{-11}	1.74×10^{-11}	2.25×10^{-11}	2.35×10^{-11}	1.78×10^{-11}	1.72×10^{-11}	1.66×10^{-11}	1.91×10^{-11}	2.31×10^{-11}
B_2	3.77×10^{-22}	4.58×10^{-23}	7.01×10^{-23}	9.25×10^{-23}	5.82×10^{-23}	5.56×10^{-23}	4.91×10^{-23}	7.39×10^{-23}	9.21×10^{-23}
$E_{rms}(\%)$	0.827	0.787	1.666	2.309	1.679	1.958	1.676	1.462	1.969

shown at the previous page, respectively. The auxiliary variables G and F are given by the following

$$G_{xy}^{n+\frac{1}{2}}\left(i,j+\frac{1}{2},k+\frac{1}{2}\right) = d_{y1}G_{xy}^{n-\frac{1}{2}}\left(i,j+\frac{1}{2},k+\frac{1}{2}\right) + d_{y2}\left[E_z^n\left(i,j+1,k+\frac{1}{2}\right) - E_z^n\left(i,j,k+\frac{1}{2}\right)\right],$$

$$G_{xz}^{n+\frac{1}{2}}\left(i,j+\frac{1}{2},k+\frac{1}{2}\right) = d_{z1}G_{xz}^{n-\frac{1}{2}}\left(i,j+\frac{1}{2},k+\frac{1}{2}\right) + d_{z2}\left[E_y^n\left(i,j+\frac{1}{2},k+1\right) - E_y^n\left(i,j+\frac{1}{2},k\right)\right],$$

$$F_{xy}^{n+1}\left(i+\frac{1}{2},j,k\right) = c_{y1}F_{xy}^{n}\left(i+\frac{1}{2},j,k\right) + c_{y2}\left[H_z^{n+\frac{1}{2}}\left(i+\frac{1}{2},j+\frac{1}{2},k\right) - H_z^{n+\frac{1}{2}}\left(i+\frac{1}{2},j-\frac{1}{2},k\right)\right],$$

$$F_{xz}^{n+1}\left(i+\frac{1}{2},j,k\right) = c_{z1}F_{xz}^{n}\left(i+\frac{1}{2},j,k\right) + c_{z2}\left[H_y^{n+\frac{1}{2}}\left(i+\frac{1}{2},j,k+\frac{1}{2}\right) - H_y^{n+\frac{1}{2}}\left(i+\frac{1}{2},j,k+\frac{1}{2}\right)\right],$$

with

$$c_{\xi 1} = \left(\frac{1-\frac{\sigma_\xi(\zeta)\Delta t}{2\varepsilon_0}}{1+\frac{\sigma_\xi(\zeta)\Delta t}{2\varepsilon_0}}\right), \quad c_{\xi 2} = \left(\frac{\frac{\sigma_\xi(\zeta)\Delta t}{\varepsilon_0\Delta\xi}}{1+\frac{\sigma_\xi(\zeta)\Delta t}{2\varepsilon_0}}\right)$$

$$d_{\xi 1} = \left(\frac{1-\frac{\sigma_\xi(\zeta+\frac{1}{2})\Delta t}{2\varepsilon_0}}{1+\frac{\sigma_\xi(\zeta+\frac{1}{2})\Delta t}{2\varepsilon_0}}\right), \quad d_{\xi 2} = \left(\frac{\frac{\sigma_\xi(\zeta+\frac{1}{2})\Delta t}{\varepsilon_0\Delta\xi}}{1+\frac{\sigma_\xi(\zeta+\frac{1}{2})\Delta t}{2\varepsilon_0}}\right).$$

Here, $\xi = y$ or z and $\zeta = j$ or k, and σ_ξ is the PML conductivity profile along the ξ-direction [11].

The implementation of parallel processing to FDTD is straightforward since FDTD involves no matrix calculation. For parallel-processing FDTD, we use the MPI library [40] that is popular and powerful for simulating large EM problems [41], [53]. In MPI-FDTD, field data should be communicated between nodes on domain decomposition interfaces. In MPI-FDTD, field data communication should be carried out for update equations relevant to Maxwell's curl equations. In our dispersive FDTD modeling, **E** field data on domain decomposition interfaces are exchanged for updating **H** (see (8)) and **H** field data on domain decomposition interfaces are exchanged for updating **D** (see (9)). We constructed a CPU cluster with 15 nodes equipped with an Intel i7-2600 (Quad Core) and 16 GB SDRAM. The total available number of processes is 60 and the total memory capacity is 240 GB. Note that the main steps of our FDTD algorithm can be summarized as

1) Save $\mathbf{G}^{n-\frac{1}{2}}$ as temporary variable.
2) Update $\mathbf{G}^{n+\frac{1}{2}}$.
3) Update $\mathbf{H}^{n+\frac{1}{2}}$.
4) Exchange $\mathbf{H}^{n+\frac{1}{2}}$ on domain decomposition interfaces.
5) Save $\mathbf{F}^n$ as temporary variable.
6) Update $\mathbf{F}^{n+1}$.
7) Update $\mathbf{D}^{n+1}$.
8) Update $\mathbf{E}^{n+1}$.
9) Exchange $\mathbf{E}^{n+1}$ on domain decomposition interfaces.

III. NUMERICAL EXAMPLES

We perform QCRF dispersion modeling for all human tissues and Table 1 summarizes QCRF coefficients and RMS errors for some representative human tissues. Fig. 5 shows the accuracy of QCRF-based electrical modeling for human skin in the frequency range of 6–100 GHz. In the figure, red solid lines indicate the QCRF dispersion model and black circles represent Gabriel's dielectric properties provided by

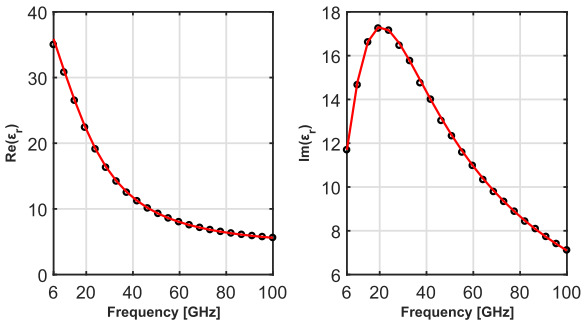

FIGURE 5. Relative permittivity of skin. Red solid lines indicate the QCRF dispersion model and black circles represent Gabriel's dielectric properties provided by IFAC [54].

Institute for Applied Physics (IFAC) [54]. The QCRF dispersion model agrees very well with Gabriel's dielectric data in the frequency of interest. In what follows, the QCRF dispersion model in Table 1 is employed for the electrical modeling of the high-resolution FDTD human voxel model.

In the following FDTD simulations, the ten layers of PML are used and the time step size is determined by the Courant-Friedrichs-Lewy (CFL) stability condition [11]. In other words, $\Delta t = CFLN\Delta s/c_0\sqrt{d}$, where c_0 is the speed of light in vacuum and d stands for the dimensionality of the problem geometry. In this work, CFL number ($CFLN$) of 0.99 is used. The excitation pulse is a sine wave modulated with Gaussian pulse with the bandwidth of 6–100 GHz, unless specified otherwise. To validate our FDTD modeling, we first consider a 1-D inhomogeneous problem that has the boundary of free space and cerebrospinal fluid. We perform FDTD simulations with the coarse FDTD cell ($\Delta x = 0.5$ mm, same as the original human phantom) and the fine FDTD cell ($\Delta x = 0.025$ mm, same as our high-resolution human phantom). A discrete Fourier transform (DFT) is used to obtain frequency-domain responses from FDTD time-domain results [55]. Fig. 6 and Fig. 7 show the reflection coefficient calculated from the FDTD simulations with $\Delta x = 0.5$ mm and $\Delta x = 0.025$ mm. In the figures, lines indicate FDTD results and symbols indicate theoretical results [56]. Very large errors are observed for the FDTD simulation with the coarse FDTD cell, because of its poor resolution. In contrast, the FDTD simulation with the refined FDTD cell has excellent agreement with theoretical results, thus illustrating the validity of the voxel resolution enhancement method.

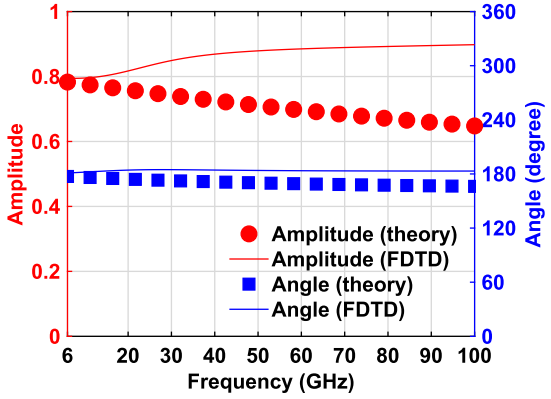

FIGURE 6. Reflection coefficient for the FDTD simulation of the original human phantom. Lines indicate FDTD results and symbols indicate theoretical results.

Before proceeding with 3-D FDTD simulations, it is of great importance to investigate the computation efficiency of MPI-based parallel FDTD. Toward this purpose. we consider one-eighth human voxel model (Fig. 4), i.e., 400 × 600 × 400 voxels. Fig. 8 shows the computation efficiency of MPI-based parallel FDTD by plotting scalability (the ratio of the computation time on one process of the computation time on many processes) [53]. As shown in the

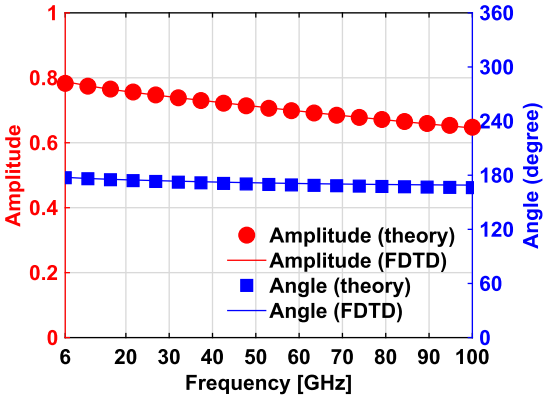

FIGURE 7. Reflection coefficient for the FDTD simulation of the high-resolution human phantom. Legends are same as Fig. 6.

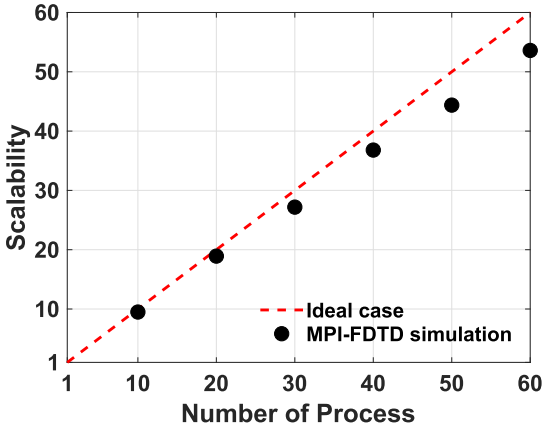

FIGURE 8. Scalability versus the number of processes.

figure, the computation efficiency increases as the number of processes increases. Note that the discrepancy between FDTD simulations and the ideal case results from network time, load imbalance between processes, etc. Now, we perform 3-D FDTD simulations under the z-polarized planewave excitation for (i) the original human voxel model (Fig. 1), (ii) the resolution-improved human voxel model (using only the voxel resolution enhancement method, Fig. 2), and (iii) the final high-resolution human voxel model (using both the voxel resolution enhancement and the image smoothing methods, (Fig. 4)). Fig. 9 shows the reflected electric field E_z in the time domain (Fig. 9a) and in the frequency domain (Fig. 9b). As shown in the figures, the FDTD result of the original human phantom is significantly different from FDTD results of the other two human voxel models. In addition, a distinct difference is observed between the resolution-improved human phantom case and the final high-resolution human phantom case. Next, we investigate electric field intensity on the xy-plane at the center of z coordinate for three human phantom models. In this case, a raised-cosine-ramped sine wave with the operating frequency of 100 GHz is excited to avoid DC offsets [57]. Fig. 10 shows the original human voxel model and its electric field distributions. The field distribution of the original human voxel model is significantly blurred due to the poor spatial resolution. Fig. 11 shows the resolution-improved

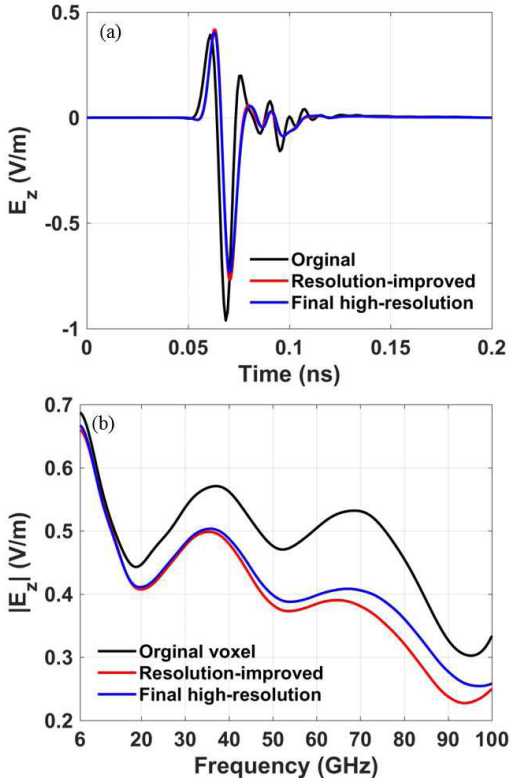

FIGURE 9. Reflected electric field E_z. (a) Time-domain response. (b) Frequency-domain response.

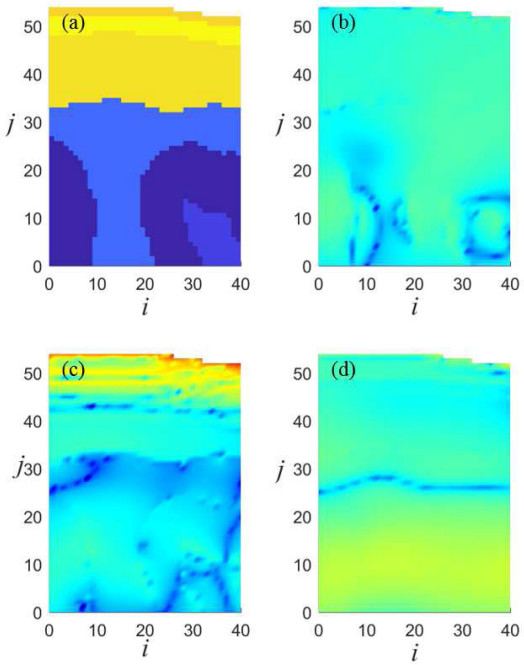

FIGURE 10. Original human voxel model on the *xy*-plane at the center of *z* coordinate. (a) Voxel. (b) E_x. (c) E_y. (d) E_z.

human voxel model and the electric field distribution in the model. Each field components agree with the geometry of the resolution-improved human voxel model because this model meets the proper voxel size at the frequency

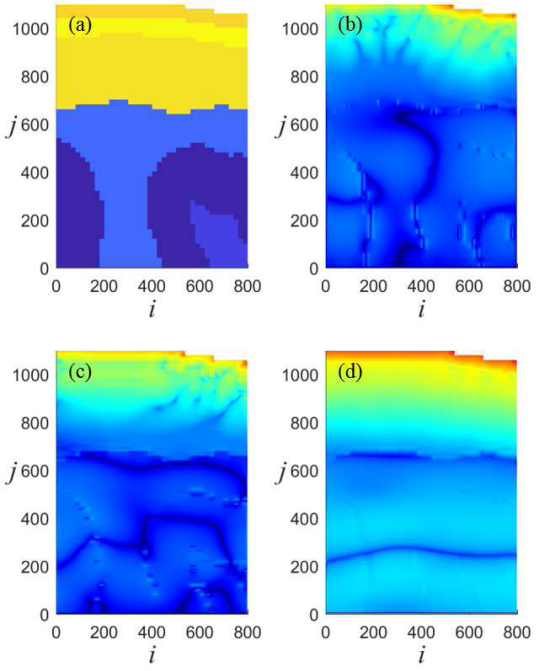

FIGURE 11. Resolution-improved human voxel model on the *xy*-plane at the center of *z* coordinate. (a) Voxel. (b) E_x. (c) E_y. (d) E_z.

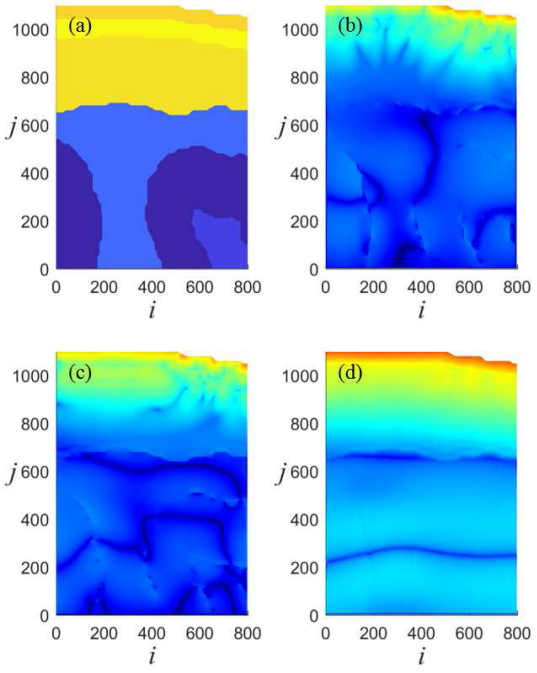

FIGURE 12. Final high-resolution human voxel model on the *xy*-plane at the center of *z* coordinate. (a) Voxel. (b) E_x. (c) E_y. (d) E_z.

of interest. However, we can observe an unnatural field distribution in some regions due to the stair-cased shape of the voxel model. These nonphysical wave flows can lead to inaccurate EM analysis. Final high-resolution human voxel model and its field distribution are shown in Fig. 12. As shown in the figures, we can observe the field distribution well according

to the tissue structure. Furthermore, weird filed distribution is not observed.

IV. CONCLUSION

We developed FDTD modeling suitable for EM analysis of human tissues at mmWave frequencies. In particular, the high-resolution human voxel model was developed for the proper geometrical modeling of a human phantom, based on the voxel resolution enhancement method and the image smoothing method. This voxel manipulation significantly improved FDTD voxel resolution and alleviated staircasing boundaries. QCRF dispersion model was successfully employed for the proper electrical modeling of human tissues in the frequency range of 6–100 GHz. The MPI parallel programming was also utilized to dramatically reduce FDTD simulation time. Numerical examples was used to illustrate the validity of our mmWave FDTD simulator. Finally, it should be noted that both geometrical and electrical modeling processes were performed only once before the FDTD time marching loop. When one considers a new frequency range and/or a new biological voxel phantom (e.g., for a child [13], a pregnant female [15], and an animal [16]), high-resolution dispersive FDTD modeling can be achieved in a similar manner presented in this work. In this work, a small region is considered, as a proof of concept. When the frequency of interest is not too high and/or the computing resources are large, the whole realistic human model can be simulated with the similar performance.

REFERENCES

[1] K. Xiong, P. Fan, Y. Zhang, and K. B. Letaief, "Towards 5G high mobility: A fairness-adjustable time-domain power allocation approach," *IEEE Access*, vol. 5, pp. 11817–11831, 2017.

[2] Y. Huo, X. Dong, and W. Xu, "5G cellular user equipment: From theory to practical hardware design," *IEEE Access*, vol. 5, pp. 13992–14010, 2017.

[3] S. Jaeckel, M. Peter, K. Sakaguchi, W. Keusgen, and J. Medbo, "5G channel model in mm-wave frequency bands," in *Proc. 22nd Eur. Wireless*, Oulu, Finland, May 2016, pp. 25–30.

[4] N. K. Nikolova, "Microwave imaging for breast cancer," *IEEE Microw. Mag.*, vol. 12, no. 7, pp. 78–94, Dec. 2011.

[5] P. Mehta, K. Chand, D. Narayanswamy, D. G. Beetner, R. Zoughi, and W. V. Stoecker, "Microwave reflectometry as a novel diagnostic tool for detection of skin cancers," *IEEE Trans. Instrum. Meas.*, vol. 55, no. 4, pp. 1309–1316, Aug. 2006.

[6] O. M. Bucci *et al.*, "Experimental framework for magnetic nanoparticles enhanced breast cancer microwave imaging," *IEEE Access*, vol. 5, pp. 16332–16340, 2017.

[7] M. Lazebnik, M. Okoniewski, J. H. Booske, and S. C. Hagness, "Highly accurate debye models for normal and malignant breast tissue dielectric properties at microwave frequencies," *IEEE Microw. Wireless Compon. Lett.*, vol. 17, no. 12, pp. 822–824, Dec. 2007.

[8] R. Aminzadeh, M. Saviz, and A. A. Shishegar, "Dielectric properties estimation of normal and malignant skin tissues at millimeter-wave frequencies using effective medium theory," in *Proc. 22nd Iranian Conf. Elect. Eng.*, Tehran, Iran, May 2014, pp. 1657–1661.

[9] C. Li, V. M. Lubecke, O. Boric-Lubecke, and J. Lin, "A review on recent advances in Doppler radar sensors for noncontact healthcare monitoring," *IEEE Trans. Microw. Theory Techn.*, vol. 61, no. 5, pp. 2046–2060, May 2013.

[10] K. Yee, "Numerical solution of initial boundary value problems involving Maxwell's equations in isotropic media," *IEEE Trans. Antennas Propag.*, vol. AP-14, no. 3, pp. 302–307, May 1966.

[11] A. Taflove and S. C. Hagness, *Computational Electrodynamics: The Finite-Difference Time-Domain Method*, 3rd ed. Norwood, MA, USA: Artech House, 2005.

[12] S. D. Gedney, *Introduction to the Finite-Difference Time-Domain (FDTD) Method for Electromagnetics*, London, U.K.: Morgan & Claypool, 2011.

[13] R. P. Findlay, A.-K. Lee, and P. Dimbylow, "FDTD calculations of SAR for child voxel models in different postures between 10 MHz and 3 GHz," *Radiat. Protection Dosimetry*, vol. 135, no. 4, pp. 226–231, Aug. 2009.

[14] C. B. Top and N. G. Gencer, "Simulation of the scattered field from a vibrating tumor inside the tissue using 3D-FDTD method," *IEEE Microw. Wireless Compon. Lett.*, vol. 23, no. 6, pp. 273–275, Jun. 2013.

[15] A. Tateno *et al.*, "Specific absorption rates of pregnant females and their fetuses from simple and realistic electromagnetic sources," *IEICE Commun. Express*, vol. 3, no. 2, pp. 55–60, Feb. 2014.

[16] J. Chakarothai, J. Wang, O. Fujiwara, K. Wake, and S. Watanabe, "A hybrid MoM/FDTD method for dosimetry of small animal in reverberation chamber," *IEEE Trans. Electromagn. Compat.*, vol. 53, no. 3, pp. 549–558, Jun. 2014.

[17] A.-K. Lee *et al.*, "Numerical implementation of representative mobile phone models for epidemiological studies," *J. Electromagn. Eng. Sci.*, vol. 16, no. 2, pp. 87–99, Apr. 2016.

[18] W. Meng and L. Qian, "MedFDTD: A parallel and open-source cross-platform framework for bioelectromagnetics field simulation," *IEEE Access*, vol. 6, pp. 12940–12944, 2018.

[19] K.-Y. Jung, B. Donderici, and F. L. Teixeira, "Transient analysis of spectrally asymmetric magnetic photonic crystals with ferromagnetic losses," *Phys. Rev. B, Condens. Matter*, vol. 74, p. 165207, Oct. 2006.

[20] K. Y. Jung, F. L. Teixeira, and R. M. Reano, "Au/SiO_2 nanoring plasmon waveguides at optical communication band," *J. Lightw. Technol.*, vol. 25, no. 9, pp. 2757–2765, Sep. 2007.

[21] G. Alsharahi, A. M. M. Mostapha, A. Faize, and A. Driouach, "Modelling and simulation resolution of ground-penetrating radar antennas," *J. Electromagn. Eng. Sci.*, vol. 16, no. 3, pp. 182–190, Jul. 2016.

[22] S.-G. Ha, J. Cho, J. Lee, B.-W. Min, J. Choi, and K.-Y. Jung, "Numerical study of estimating the arrival time of UHF signals for partial discharge localization in a power transformer," *J. Electromagn. Eng. Sci.*, vol. 18, no. 2, pp. 94–100, Apr. 2018.

[23] J.-H. Kweon, M.-S. Park, J. Cho, and K.-Y. Jung, "FDTD analysis of electromagnetic wave propagation in inhomogeneous ionosphere under arbitrary-direction geomagnetic field," *J. Electromagn. Eng. Sci.*, vol. 18, no. 3, pp. 212–214, Jul. 2018. .

[24] M. Zankl *et al.*, "The construction of computer tomographic phantoms and their application in radiology and radiation protection," *Radiat. Environ. Biophys.*, vol. 27, no. 2, pp. 153–164, Jun. 1988.

[25] I. G. Zubal, C. R. Harrell, E. O. Smith, Z. Rattner, G. Gindi, and P. B. Hoffer, "Computerized three-dimensional segmented human anatomy," *Med. Phys.*, vol. 21, no. 2, pp. 299–302, 1994.

[26] X. G. Xu, T. C. Chao, and A. Bozkurt, "VIP-Man: An image-based whole-body adult male model constructed from color photographs of the Visible Human Project for multi-particle Monte Carlo calculations," *Health Phys.*, vol. 78, no. 5, pp. 476–486, May 2000.

[27] T. Nagaoka *et al.*, "Development of realistic high-resolution whole-body voxel models of Japanese adult males and females of average height and weight, and application of models to radio-frequency electromagnetic-field dosimetry," *Phys. Med. Biol.*, vol. 49, no. 1, pp. 1–15, Jan. 2004.

[28] C. Lee, J. Lee, and C. Lee, "Korean adult male voxel model KORMAN segmented from magnetic resonance images," *Med. Phys.*, vol. 31, no. 5, pp. 1017–1022, May 2004.

[29] J. Becker, M. Zankl, U. Fill, and C. Hoeschen, "Katja—The 24^{th} week of virtual pregnancy for dosimetric calculations," *Polish J. Med. Phys. Eng.*, vol. 14, no. 1, pp. 13–19, Jan. 2008.

[30] B. Zhang, J. Ma, L. Liu, and J. Cheng, "CNMAN: A Chinese adult male voxel phantom constructed from color photographs of a visible anatomical data set," *Radiat. Protection Dosimetry*, vol. 124, no. 2, pp. 130–136, May 2007.

[31] A. Christ *et al.*, "The Virtual Family–development of surface-based anatomical models of two adults and two children for dosimetric simulations," *Phys. Med. Biol.*, vol. 55, no. 2, pp. N23–N38, Jan. 2010.

[32] Y. Wu *et al.*, "Development of Chinese female computational phantom Rad-Human and its application in radiation dosimetry assessment," *Nucl. Technol.*, vol. 201, no. 2, pp. 155–164, Feb. 2018.

[33] J. S. Park, Y. W. Jung, H.-D. Choi, and A.-K. Lee, "VK-phantom male with 583 structures and female with 459 structures, based on the sectioned images of a male and a female, for computational dosimetry," *J. Radiat. Res.*, vol. 59, no. 3, pp. 338–380, May 2018.
[34] R. C. Gonzalez and R. E. Woods, *Digital Image Processing*, 3rd ed. London, U.K.: Pearson, 2005.
[35] K. Alkhalifeh, G. Hislop, N. A. Ozdemir, and C. Craeye, "Efficient MoM simulation of 3-D antennas in the vicinity of the ground," *IEEE Trans. Antennas Propag.*, vol. 64, no. 12, pp. 5335–5344, Dec. 2016.
[36] S. Sandeep, J.-M. Jin, and C. Caloz, "Finite-element modeling of metasurfaces with generalized sheet transition conditions," *IEEE Trans. Antennas Propag.*, vol. 65, no. 5, pp. 2413–2420, May 2017.
[37] G. Scarella *et al.*, "Realistic numerical modelling of human head tissue exposure to electromagnetic waves from cellular phones," *Comp. Rendus Physique*, vol. 7, no. 5, pp. 501–508, Jun. 2006.
[38] H. Tankaria *et al.*, "VHP-Female full-body human CAD model for cross-platform FEM simulations—Recent development and validations," in *Proc. IEEE 38th Annu. Int. Conf. Eng. Med. Biol. Soc.*, Orlando, FL, USA, Aug. 2016, pp. 2232–2235.
[39] S.-G. Ha, J. Cho, J. Choi, H. Kim, and K.-Y. Jung, "FDTD dispersive modeling of human tissues based on quadratic complex rational function," *IEEE Trans. Antennas Propag.*, vol. 61, no. 2, pp. 996–999, Feb. 2013.
[40] Argonne National Laboratory. *MPICH (MPI Chameleon)*. Accessed: May 1, 2017. [Online]. Available: http://www.mcs.anl.gov
[41] S.-M. Park, E.-K. Kim, Y. B. Park, S. Ju, and K.-Y. Jung, "Parallel dispersive FDTD method based on the quadratic complex rational function," *IEEE Antennas Wireless Propag. Lett.*, vol. 15, pp. 425–428, 2016.
[42] M. Fujii, "Maximum frequency range limit of multi-pole Debye models of human body tissues," *IEEE Microw. Wireless Compon. Lett.*, vol. 22, no. 2, pp. 73–75, Feb. 2012.
[43] K. Y. Jung and F. L. Teixeira, "Multispecies ADI-FDTD algorithm for nanoscale three-dimensional photonic metallic structures," *IEEE Photon. Technol. Lett.*, vol. 19, no. 8, pp. 586–588, Apr. 15, 2007.
[44] H. Chung, J. Cho, S.-G. Ha, S. Ju, and K.-Y. Jung, "Accurate FDTD dispersive modeling for concrete materials," *ETRI J.*, vol. 35, no. 5, pp. 915–918, Oct. 2013.
[45] H. Chung, K.-Y. Jung, X. T. Tee, and P. Bermel, "Time domain simulation of tandem silicon solar cells with optimal textured light trapping enabled by the quadratic complex rational function," *Opt. Express*, vol. 22, no. S3, pp. A818–A832, Apr. 2014.
[46] E. Kim, S.-G. Ha, J. Lee, Y. B. Park, and K.-Y. Jung, "Three-dimensional efficient dispersive alternating-direction-implicit finite-difference time-domain algorithm using a quadratic complex rational function," *Opt. Express*, vol. 23, no. 2, pp. 873–881, Jan. 2015.
[47] E. C. Levy, "Complex-curve fitting," *IRE Trans. Autom. Control*, vol. AC-4, no. 1, pp. 37–44, May 1959.
[48] H. Chung, S.-G. Ha, J. Choi, and K.-Y. Jung, "Accurate FDTD modelling for dispersive media using rational function and particle swarm optimisation," *Int. J. Electron.*, vol. 102, no. 7, pp. 1218–1228, Jul. 2015.
[49] W. H. Weedon and C. M. Rappaport, "A general method for FDTD modeling of wave propagation in arbitrary frequency-dispersive media," *IEEE Trans. Antennas Propag.*, vol. 45, no. 3, pp. 401–410, Mar. 1997.
[50] S.-G. Ha, J. Cho, E.-K. Kim, Y. B. Park, and K.-Y. Jung, "FDTD dispersive modeling with high-order rational constitutive parameters," *IEEE Trans. Antennas Propag.*, vol. 63, no. 9, pp. 4233–4238, Sep. 2015.
[51] W. C. Chew and W. H. Weedon, "A 3D perfectly matched medium from modified Maxwell's equations with stretched coordinates," *Microw. Opt. Technol. Lett.*, vol. 7, no. 13, pp. 599–604, Sep. 1994.
[52] K.-Y. Jung, S. Ju, and F. L. Teixeira, "Application of the modal CFS-PML-FDTD to the analysis of magnetic photonic crystal waveguides," *IEEE Microw. Wireless Compon. Lett.*, vol. 21, no. 4, pp. 179–181, Apr. 2011.
[53] C. Guiffaut and K. Mahdjoubi, "A parallel FDTD algorithm using the MPI library," *IEEE Antennas Propag. Mag.*, vol. 43, no. 2, pp. 94–103, Apr. 2001.
[54] D. Andreuccetti, R. Fossi, and C. Petrucci. *Dielectric Properties of Body Tissues*. [Online]. Available: http://niremf.ifac.cnr.it/tissprop/
[55] C. M. Fuse and O. P. Gandhi, "Why the DFT is faster than the FFT for FDTD time-to-frequency domain conversions," *IEEE Microw. Guided Wave Lett.*, vol. 5, no. 10, pp. 326–328, Oct. 1995.
[56] C. A. Balanis, *Advanced Engineering Electromagnetics*, 2nd. ed. Hoboken, NJ, USA: Wiley, 2012.
[57] C. M. Furse, D. H. Roper, D. N. Buechler, D. A. Christensen, and C. H. Durney, "The problem and treatment of DC offsets in FDTD simulations," *IEEE Trans. Antennas Propag.*, vol. 48, no. 8, pp. 1198–1201, Aug. 2000.

JAE-WOO BAEK received the B.S. degree in electronics and information engineering from Korea University, Sejong, South Korea, in 2015, and the M.S. degree in electrical engineering from Hanyang University, Seoul, South Korea, in 2017, where he is currently pursuing the Ph.D. degree in electrical and computer engineering. His current research interests include computational electromagnetics, bioelectromagnetics, and parallel programming.

DONG-KYOO KIM received the Ph.D. degree in electronics and computer engineering from the Pohang University of Science and Technology, South Korea, in 2004. He was a Visiting Researcher with the Georgia Institute of Technology, Atlanta, USA, in 2004. Since 2005, he has been with the Electronics and Telecommunications Research Institute, Daejeon, South Korea, as a Senior Researcher. His current research interests include ground/wall penetrating radar, vital signal sending radar, and other remote sensing and imaging technologies, indoor localization technologies, wireless communication systems, and the IoT sensor devices.

KYUNG-YOUNG JUNG (SM'13) received the B.S. and M.S. degrees in electrical engineering from Hanyang University, Seoul, South Korea, in 1996 and 1998, respectively, and the Ph.D. degree in electrical and computer engineering from The Ohio State University, Columbus, USA, in 2008.

From 2008 to 2009, he was a Post-Doctoral Researcher with The Ohio State University, and from 2009 to 2010, he was an Assistant Professor with the Department of Electrical and Computer Engineering, Ajou University, Suwon, South Korea. Since 2011, he has been with Hanyang University, where he is currently an Associate Professor with the Department of Electronic Engineering. His current research interests include computational electromagnetics, bioelectromagnetics, and nano-electromagnetics. He is an Associate Editor of the *IEICE Transactions on Communications*.

Dr. Jung was a recipient of the Graduate Study Abroad Scholarship from the National Research Foundation of Korea, the Presidential Fellowship from The Ohio State University, the Best Teacher Award from Hanyang University, and the Outstanding Research Award from the Korean Institute of Electromagnetic Engineering Society.